SPECIAL
DYNAMO/CINDY/AMIE/LASP
COLLECTION

AIRCRAFT OBSERVATIONS OF DRY AIR, THE ITCZ, CONVECTIVE CLOUD SYSTEMS, AND COLD POOLS IN MJO DURING DYNAMO

BY SHUYI S. CHEN, BRANDON W. KERNS, NICK GUY, DAVID P. JORGENSEN, JULIEN DELANOË, NICOLAS VILTARD, CHRISTOPHER J. ZAPPA, FALKO JUDT, CHIA-YING LEE, AND AJDA SAVARIN

The DYNAMO airborne measurements provide new insights into the distinct characteristics of convection, cold pools, water vapor, and air–sea fluxes from the suppressed to active phases of MJO initiation in the Indian Ocean.

The Madden–Julian oscillation (MJO; Madden and Julian 1971, 1972) is known to have a major impact on global weather systems, such as heat waves, tropical cyclones, and winter storms (e.g., Maloney and Hartmann 2000; Zhou et al. 2012). The intraseasonal/planetary time and spatial scales of the MJO make it a critical link between the global weather and climate systems (Zhang 2013). However, current global weather and climate models have little skill in predicting the MJO. The convective initiation of the MJO over the Indian Ocean, which typically consists of suppressed, onset, and active phases of the large-scale equatorial convection (Stephens et al. 2004; Yoneyama et al. 2013), is one of the most challenging problems in predicting the MJO (e.g., Benedict and Randall 2009). A major international field campaign supported by the Dynamics of the Madden–Julian Oscillation (DYNAMO), the Cooperative Indian Ocean Experiment on Intraseasonal Variability (CINDY), the Atmospheric Radiation Measurement Program (ARM) MJO Investigation Experiment (AMIE), and the Littoral Air–Sea Processes (LASP) programs took place over the Indian Ocean with an intensive observing period (IOP) from 1 October 2011 to 15 January 2012 (Yoneyama et al. 2013). Three MJO events were observed during the IOP of the field program (DYNAMO). A detailed description of the MJO events during DYNAMO can be found in Gottschalck et al. (2013). Here we focus on key observations from aircraft measurements collected during the MJO initiation over the tropical Indian Ocean from November to December 2011.

SCIENCE OBJECTIVES AND MEASUREMENTS OF THE AIRCRAFT MISSIONS IN DYNAMO. The aircraft missions aimed to address three main science objectives of DYNAMO to better understand 1) multiscale convection–environment interactions, 2) water vapor variability and three-dimensional (3D) dynamical and microphysical structure in convective cloud systems, and 3) air–sea fluxes and boundary layer structure in the MJO initiation over the Indian Ocean. The flights were

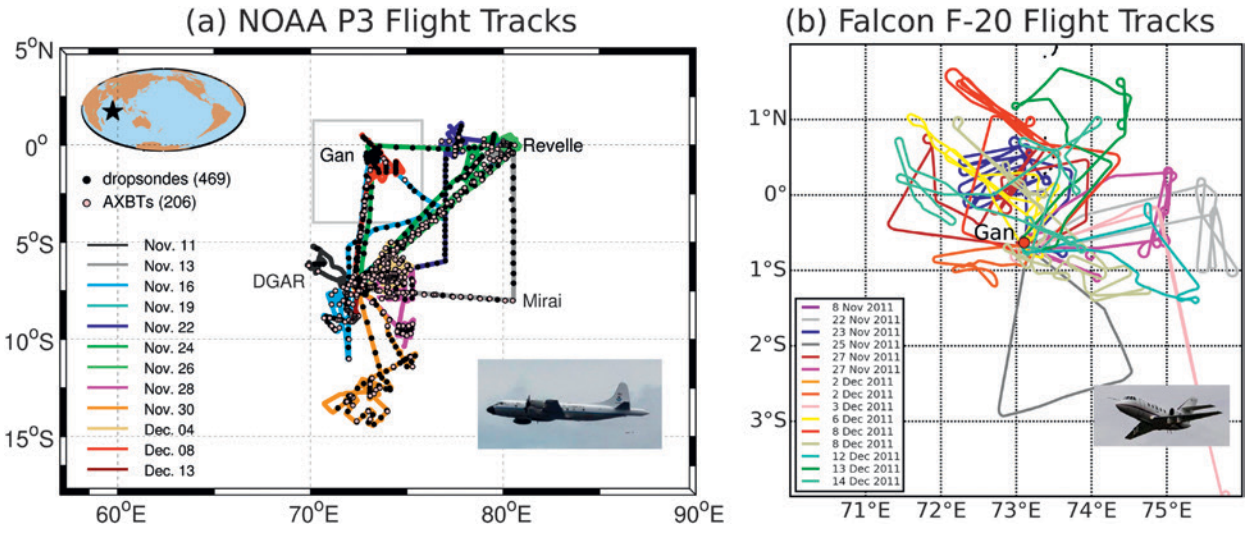

Fig. 1. (a) The NOAA WP-3D aircraft [stationed at Diego Garcia (DGAR)] flight tracks of the 12 missions from 11 Nov to 13 Dec 2011 during DYNAMO. The black dots and open circles indicate air-deployed GPS dropsonde and AXBT locations, respectively. (b) The French Falcon 20 aircraft (stationed at Gan Island) flight tracks of the 15 missions from 22 Nov to 16 Dec 2011 over the region near Gan as marked by the inset in (a). The aircraft missions are color coded by dates.

designed to sample the MJO initiation processes including convective cloud systems and their atmospheric and oceanic environment during all MJO phases, from the convectively suppressed phase to the active phase. This sampling strategy allowed us to address one of the most challenging problems in MJO initiation: the multiscale interaction among convective cloud systems, their large-scale environment, and the upper ocean on time scales from hours to weeks. Summaries of the National Oceanic and Atmospheric Administration (NOAA) WP-3D and French Falcon 20 aircraft flights, specific objectives, and key measurements of each mission are given in Tables ES1 and ES2, respectively, in the online supplement.

The two aircraft provided finescale, dynamic, mobile measurements to sample the gaps between the stationary ground and ship sites that formed the DYNAMO arrays (Fig. 1). The WP-3D actively pursued the largest convective systems in the DYNAMO domain during the convective missions using primarily its vertically scanning Doppler radar (Jorgensen et al. 1996, 1997). The flight strategies contained various aircraft tracks, including one that allowed the analysis of mesoscale convective systems (MCSs) during each roughly hour-long portion from the Doppler radar reflectivity and velocity (Guy and Jorgensen 2014) and microphysics probes (N. Guy et al. 2015, personal communication). Other WP-3D flight tracks focused on the large-scale environmental conditions, including water vapor, temperature, and winds from transects between the island and ship sites (Kerns and Chen 2014b); the coupled atmosphere–ocean boundary layers; convectively generated cold pools and air–sea fluxes using the global positioning system (GPS) dropsondes; the airborne expendable bathythermographs (AXBTs); and the downward-looking infrared (IR) imaging spectrometer called the Japanese Dynamic Earth Observation by Very Long Baseline Interferometer (JADE) (Table ES1). The French Falcon 20 operated by Service des Avions Français Instrumentés pour la Recherche en Environnement

AFFILIATIONS: Chen, Kerns, Judt, and Savarin—Rosenstiel School of Marine and Atmospheric Science, University of Miami, Miami, Florida; Guy—University of Wyoming, Laramie, Wyoming; Jorgensen—NOAA/National Severe Storms Laboratory, Norman, Oklahoma; Delanoë and Viltard—LATMOS, L'Institut Pierre-Simon Laplace, Guyancourt, France; Zappa—Lamont-Doherty Earth Observatory, Columbia University, Palisades, New York; Lee—International Research Institute for Climate and Society, Columbia University, Palisades, New York
CORRESPONDING AUTHOR: Dr. Shuyi S. Chen, RSMAS, University of Miami, 4600 Rickenbacker Causeway, Miami, FL 33149
E-mail: schen@rsmas.miami.edu

The abstract for this article can be found in this issue, following the table of contents.
DOI:10.1175/BAMS-D-13-00196.1

A supplement to this article is available online (10.1175/BAMS-D-13-00196.2)

In final form 26 May 2015

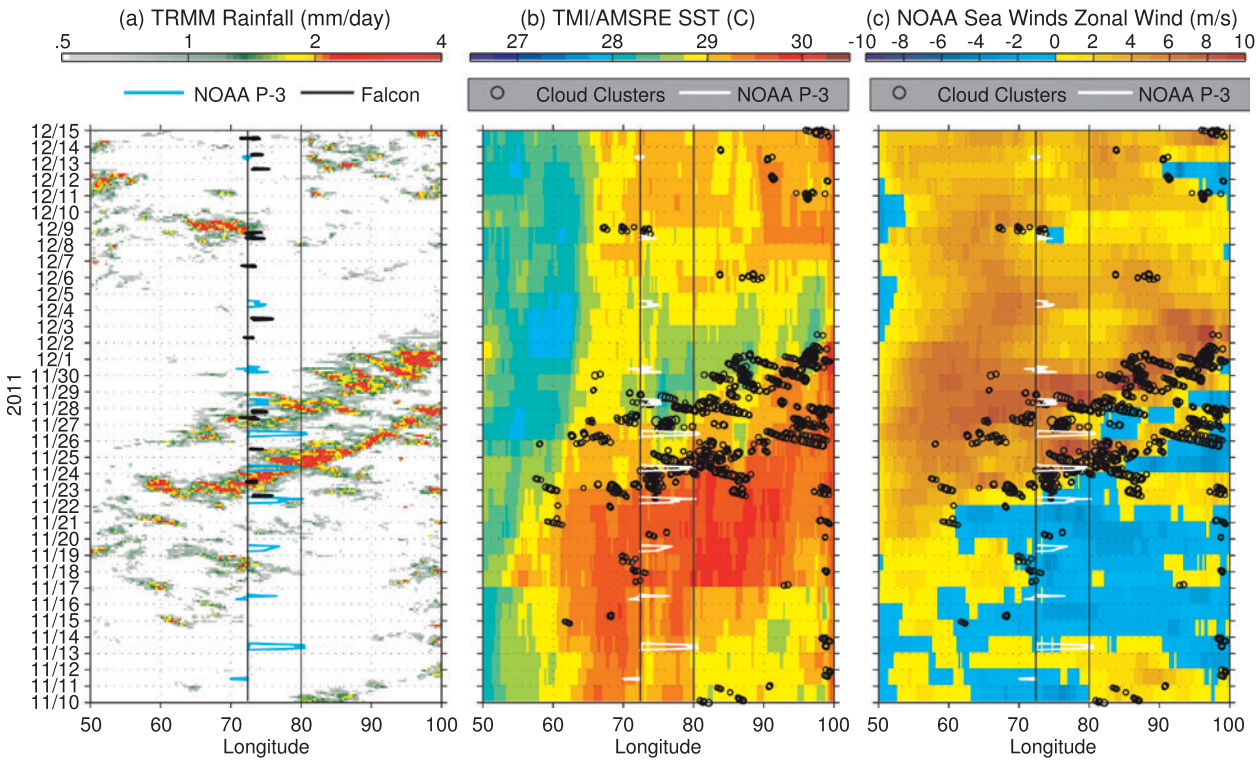

Fig. 2. Time–longitude diagrams of (a) TRMM 3B42 rain rate (color, mm day^{-1}), (b) TRMM/AMSR-E SST (color, °C) overlaid with cloud clusters from *Meteosat-7* IR data, and (c) NOAA SeaWinds zonal surface wind (color, m s^{-1}) from 10 Nov to 15 Dec 2011. The rain rate, SST, and zonal winds are averaged within the tropical latitude zone between 5°S and 5°N. The IR cloud clusters [cloud-top temperature < 208 K] are within the same latitude zone. The size of the black circles is proportional to the size of the observed cloud clusters. The DYNAMO-observing array is within the region between the blue lines (72°–80°E). The WP-3D aircraft tracks are marked in blue in (a) and white in (b) and (c). The Falcon 20 flight tracks are shown by black lines in (a).

(SAFIRE) was equipped with a millimeter-wave Doppler cloud radar and a set of microphysics in situ probes along with the usual environmental measurements (e.g., temperature, relative humidity, and winds; Table ES2). The Falcon 20 aircraft flew mostly near Gan Island (Fig. 1b) and focused on the upper-troposphere ice cloud properties in MCSs. Collectively the two aircraft provided the most comprehensive suite of observations of combined Doppler radar reflectivity and velocity from the lower to the upper troposphere, microphysical properties, convective cold pools, and air–sea fluxes from the GPS dropsondes and AXBTs in tropical oceanic MCSs to date.

LARGE-SCALE CONTEXT OF THE AIRCRAFT OBSERVATIONS. A strong MJO initiation event was observed from 10 November to 15 December 2011 (Yoneyama et al. 2013). An objective cloud-cluster tracking analysis using hourly *Meteosat-7* IR data (based a method described in Chen et al. 1996; Chen and Houze 1997a,b), along with the Tropical Rainfall Measuring Mission (TRMM) 3B42 rain rate (Huffman et al. 2007), the Advanced Microwave Scanning Radiometer for Earth Observing System (AMSR-E) sea surface temperature (SST), the NOAA SeaWinds surface wind data (Zhang et al. 2006), and the DYNAMO in situ observations, provides a four-dimensional description of the multiscale variability of convective cloud systems and the air–sea fluxes in relation to the MJO initiation over the Indian Ocean. Figure 2 shows the eastward propagation of the large-scale envelope of TRMM precipitation and convective cloud clusters (IR cloud-top temperature < 208 K), changes in SST, and surface winds during the MJO. The cloud clusters became more numerous and increased in size as each MJO event developed. Prior to the onset of the convectively active phase of the MJO in late November 2011, the DYNAMO array is characterized by relatively warm SST and easterly winds (Figs. 2b and 2c). Significant SST cooling and strong near-surface westerly winds occurred during and after the convectively active phase from 25 November to early December. The convective cloud systems are highly correlated with features in the

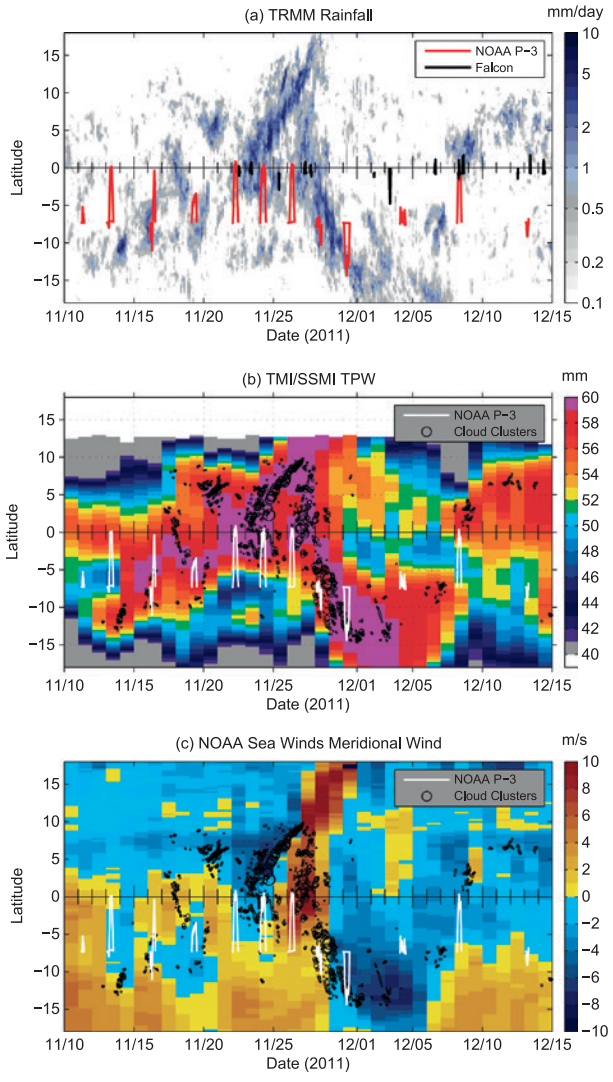

Fig. 3. Time–latitude diagrams of (a) the TRMM 3B42 rain rate (mm day^{-1}), (b) TPW (mm), and (c) NOAA SeaWinds meridional wind component (m s^{-1}) averaged over the DYNAMO array longitude 72°–80°E from 10 Nov to 15 Dec 2011. The black circles are the IR (<208 K) cloud clusters. The size of circles is proportional to the size of the cloud clusters. The WP-3D aircraft tracks are marked in red in (a) and white in (b) and (c). The Falcon 20 flight tracks are shown in black lines in (a).

surface winds from the meso and synoptic scale to intraseasonal time scales as seen in the NOAA SeaWinds zonal wind (Fig. 2c), including a complex mix of both local and remote large-scale conditions and impacts of these systems.

The eastward-propagating large-scale convection had two maxima (Fig. 2a). The first one represents the leading edge of the large convective envelope of the MJO (see Fig. 9 in Johnson and Ciesielski 2013). It has been described as being associated with a convectively coupled Kelvin wave in Gottschalck et al. (2013). The second maximum consisted of mostly westward-propagating large precipitating cloud clusters that may be associated with the equatorial Rossby waves and mixed Rossby–gravity waves (Kiladis et al. 2009). One of the largest westward-propagating systems occurred on 28 November over the DYNAMO array, which was described in detail by Judt and Chen (2014). The distinct rainfall minimum between the two maxima (Fig. 2a) is due to dry air advecting into the equatorial region by Rossby wave gyres that were continually generated as part of the large-scale convective complex of the MJO (Kerns and Chen 2014a,b).

Another interesting feature is the transition of the large-scale convective activity from the intertropical convergence zone (ITCZ) to the equator during MJO initiation (Fig. 3a). Prior to the onset of the equatorial convective activity, deep convection was concentrated within the ITCZ near 8°–10°S (Fig. 3a). The convection shifted toward the equator in mid-November. An abrupt northward jump from the ITCZ to the equator occurred on 22 November when a strong dry air intrusion [minimum total precipitable water (TPW) between 5° and 10°S] from the subtropical region south of the DYNAMO array intruded north to 5°S of the equator (Fig. 3b). The dry air intrusion is associated with a maximum in the southerly (equatorward) wind from 15° to 5°S on 21–23 November (Fig. 3c), and with the group of long-lasting, northward-propagating clusters and the associated anomalous northerlies–southerlies couplet (meridional confluence zone) north of the equator from 24 to 27 November (Fig. 3c). These features mark a Rossby Gyre that developed in the active phase of the MJO, which later become Tropical Cyclone 5 (Moum et al. 2014). Another southerly dry air intrusion occurred from 8 to 15 December (Figs. 3b and 3c) but apparently with a less favorable equatorial environment for widespread deep convection in that case.

The WP-3D aircraft sampled all phases of the MJO as well as the ITCZ from 11 November to 13 December, while the Falcon 20 observations captured the convectively active and suppressed phases from 22 November to 14 December near Gan Island, as shown in Figs. 1–3. Examples of the aircraft observations from various large-scale conditions during the MJO initiation are presented in the follow sections.

CONVECTIVE CLOUD SYSTEMS IN SUPPRESSED, TRANSITION, AND ACTIVE PHASES OF MJO.

Tropospheric moisture is a major parameter affecting convection during MJO initiation (Kerns and Chen 2014b). Satellite and rawinsonde

observations suggest that synoptic-scale dry air advection plays an important role in convective suppression in the tropics (Yoneyama and Parsons 1999; Kerns and Chen 2014b). The synoptic-scale variability in the wind and the atmospheric moisture fields is a key feature distinct from the different global model forecasts of the late November MJO initiation event during DYNAMO (Kerns and Chen 2014a). Moreover, the interactive processes between convective cloud systems and their large-scale environmental moisture on various scales—for example, equatorial waves—are not well understood. Here we use the WP-3D Doppler radar and the GPS dropsonde data together with the cloud-cluster tracking analysis using hourly *Meteosat-7* IR data and satellite-observed TPW to provide a four-dimensional description of the multiscale variability of environmental moisture and convective cloud systems during this MJO initiation. Observations from four WP-3D aircraft missions are shown covering the entire MJO initiation from the convectively suppressed phase on 13 November (Fig. 4a), the transition/onset phase on 22 November (Fig. 4b), the active phase on 24 November (Fig. 4c), and the return to the suppressed phase on 8 December

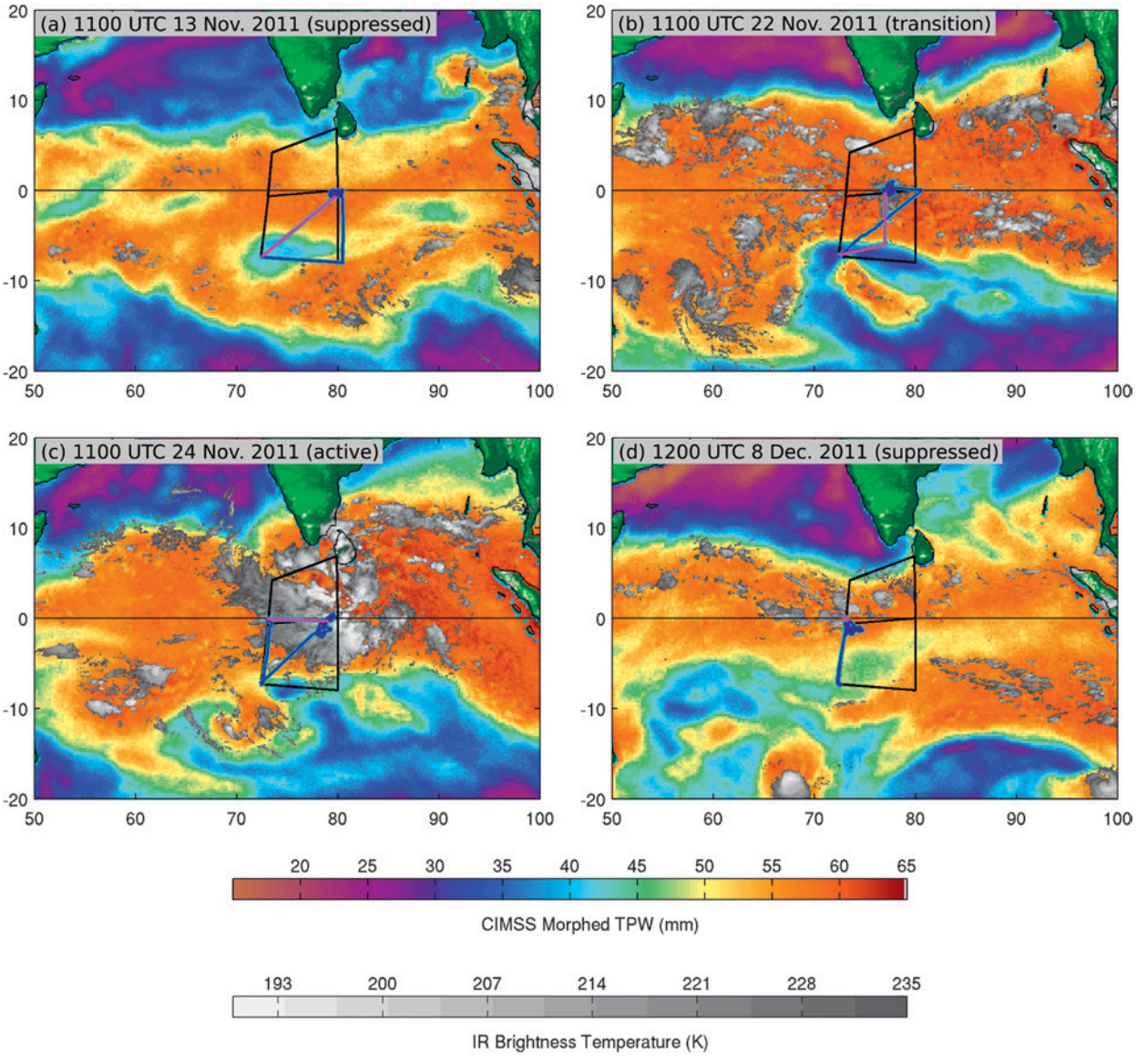

Fig. 4. TPW (color, mm) from the Cooperative Institute for Meteorological Satellite Studies (CIMMS) morphed product and the Meteosat IR brightness temperatures (gray, K) for four aircraft missions: (a) 13 Nov (suppressed), (b) 22 Nov (transition), (c) 24 Nov (active), and (d) 8 Dec 2011 (suppressed). The DYNAMO array is drawn in black lines. The WP-3D flight tracks are shown in blue lines. Detailed observations along the flight leg highlighted in magenta will be shown in Figs. 5–8, 12, and 13.

(Fig. 4d). The following three subsections describe the aircraft observations from the transition/onset, active, and suppressed phases of the MJO.

Dry air, ITCZ, and transition from convectively suppressed to active phase of MJO. To address the question of convective organization and its interaction with the large-scale environment during MJO initiation, observations of convective cloud systems and their immediate surrounding environmental moisture were measured by the airborne Doppler radar, the GPS dropsondes, and flight-level measurements on board the WP-3D aircraft. During the onset of equatorial convection at the early stage of the MJO event from 20 to 23 November, dry air intrusion from the extratropical regions may be instrumental in disrupting the southern ITCZ

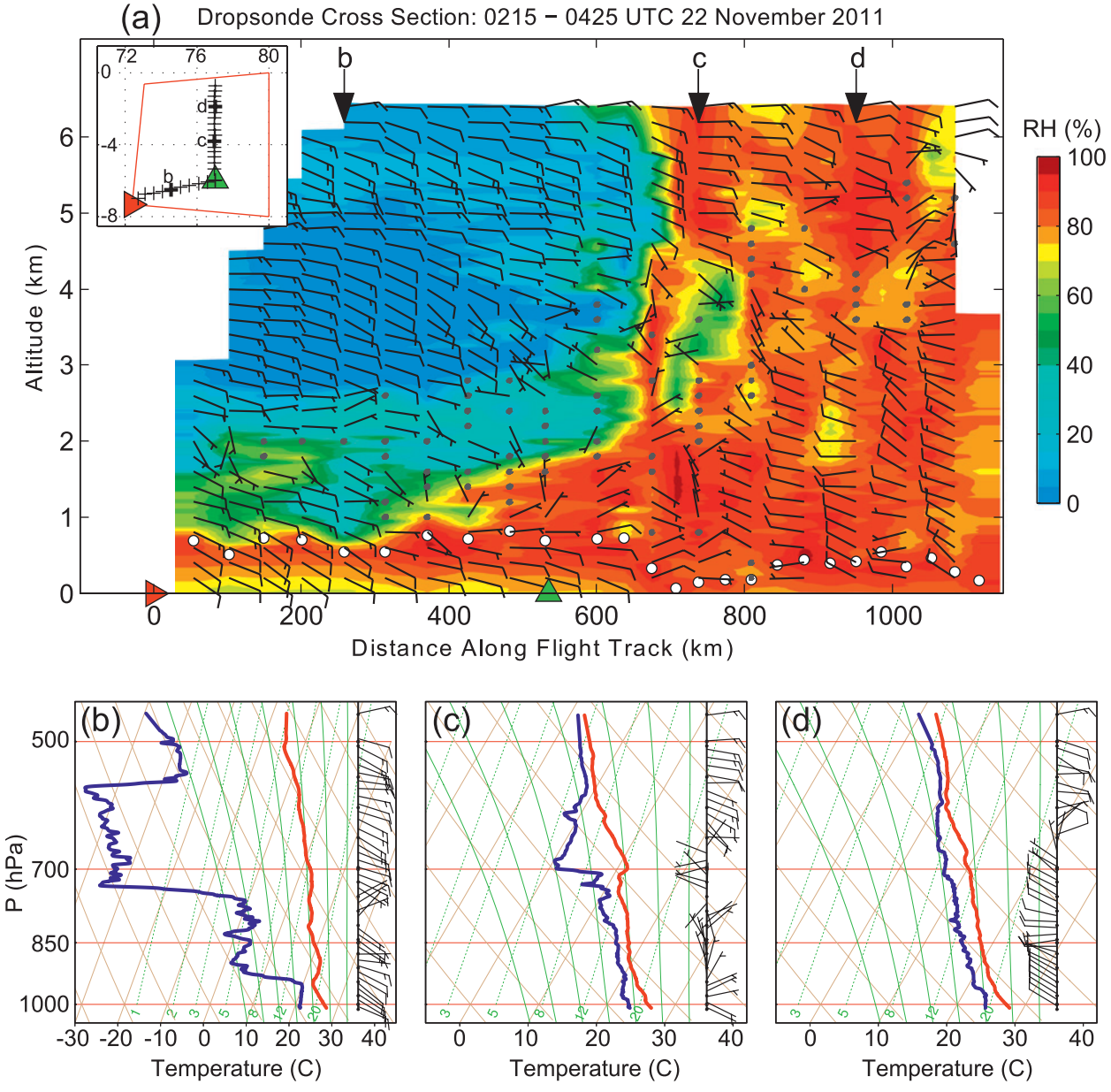

Fig. 5. Dry air intrusion during the transition from the convectively suppressed phase to the active phase of the MJO on 22 Nov 2011 (see Fig. 4b). (a) RH (%) and wind measured by the GPS dropsondes along the WP-3D aircraft track shown on the map (inset) with corresponding locations marked by red and green triangles and dropsonde locations at the black arrows at "b," "c," and "d." White dots represent the height of the atmospheric boundary layer. (b)–(d) Skew *T*–log*p* diagrams from dropsondes deployed at three locations marked by the black arrows in (a), showing the contrasting dry air in the south and moist air near the equator. Wind barbs in (a)–(d) show the direction and wind speed of the horizontal wind. Each flag represents 5 m s^{-1} [~10 knots (kt); 1 kt = 0.51 m s^{-1}].

RAIN, COLD POOLS, AND SEA STATES DURING THE SUPPRESSED AND ACTIVE PHASES OF THE MJO

Rain-induced freshwater pools on the ocean surface and the atmospheric cold pools from convective downdraft driven by evaporation of precipitation can modulate air–sea fluxes and the atmospheric stability that in turn affect convective variability. During the suppressed phase of the MJO, convective rain showers produce cool freshwater lenses over the ocean surface in low-wind conditions (Fig. SB1, top). The SST variability in the vicinity of the rain cell shown in Fig. SB1 (top) was captured by the WP-3D aircraft during the DYNAMO field campaign on 16 November 2011 (Fig. 11). Although it is well known that convective rain cells—such as the one shown in Fig. SB1 (top)—are numerous, the spatial and temporal scales of the cool freshwater pools and how they may affect the SST and air–sea fluxes are difficult to quantify. In contrast, during the active phase of the MJO, large convective mesoscale systems produced an extensive and deep layer of cold pools from the ocean surface to the atmospheric surface and boundary layers (or above in some cases). Strong winds induced surface waves and white caps (Fig. SB1, bottom) produce strong mixing in the upper ocean and enhanced air–sea fluxes during the active phase of the MJO. The contrasting air–sea interaction processes in the suppressed and active phases of the MJO and their impact on the evolution of MJO initiation need further investigation.

Fig. SB1. (top) Clouds, rain, and calm sea surface during the WP-3D flight near Gan Island on 16 Nov when surface wind speeds were <5 m s^{-1}. (bottom) Sea surface waves and white caps observed during the WP-3D flight near R/V *Revelle* on 24 Nov when surface wind speeds were >15–20 m s^{-1} during the DYNAMO field campaign over the equatorial Indian Ocean. (Photos by Shuyi S. Chen.)

and forcing convection toward the equator (Kerns and Chen 2014b). Figure 5 shows an example of the dry air and a strong relative humidity (RH) gradient observed by the GPS dropsondes on 22 November, when the convection moved toward the equatorial region in response to the dry air intrusion from the south. The WP-3D flew through the dry air mass on its way to sample the convective cloud systems near the equator (Fig. 4b). The extreme low values of RH < 10% were observed in the low–midtroposphere near 4°–5°S (Fig. 5a). Prior to 22 November, the convection in the southern ITCZ was active near 10°S (Fig. 3). This dry air intrusion was found to be responsible for "pushing" convective activity from the southern ITCZ to the equator during the transition/onset of the MJO convective phase (Kerns and Chen 2014b). The GPS dropsondes deployed from WP-3D provided in situ observations of the large-scale environmental moisture and winds as well as the atmosphere boundary layer structure. The depth of the atmosphere boundary layer (defined by the mixed layer using 0.5-K virtual potential temperature gradient) is higher in the dry air region (600–800 km) and lower in the moist region from 5°S to the equator (below 400–500 km) as shown by the white dots in Fig. 5a. The lower-tropospheric wind is easterly in the southern portion of the DYNAMO array with a relatively strong southeasterly component observed by the dropsonde near 7°S, 75°E (Fig. 5a) corresponding to the dry air intrusion (Fig. 4b). The winds changed to low–midtropospheric westerlies from about 4°S to the equator with a transition zone from 6° to 4°S, where a relatively weak midlevel westerly was observed in between the lower- and upper-tropospheric easterlies (Fig. 5a).

The distinct vertical moisture and wind profiles from the extremely dry air environment to the nearly saturated region close to the equator as well as the transition zone are shown clearly by skew T–log$p$ diagrams from the WP-3D transect on 22 November (Fig. 5). The dry air region was dominated by a relatively strong, deep layer of easterlies, with RH as low as ~10% above 800 hPa (Fig. 5b), whereas the equatorial region had low–midlevel westerlies and upper-level easterlies with RH greater than 90% through a deep layer (Fig. 5d). The sounding collected in the transition zone between the dry and moist areas displayed an interesting "onion"-shaped temperature and dewpoint temperature profile (indicative of subsidence) between 600 and 700 hPa below a nearly saturated melting layer as well as a midlevel westerly wind (Fig. 5c), which displayed a somewhat similar property to those observed in the stratiform rain region of MCSs (e.g., Zipser 1977)

Convective cloud systems and enhanced surface winds in the active phase. Organized MCSs can interact with their large-scale environment through the vertical transport of heat, moisture, and momentum. Previous observations and modeling studies have shown that tropical MCSs can enhance surface westerlies in the MJO during the Tropical Ocean and Global Atmosphere Coupled Ocean–Atmosphere Response Experiment (TOGA COARE; e.g., Houze et al. 2000; Mechem et al. 2005). Midlevel inflow jets developed in the large MCSs can enhance the surface westerlies through melting and evaporative-cooling-driven downward motion and momentum transport in the active phase of the MJO (Jorgensen et al. 1997). During DYNAMO, the onset of the active phase of the MJO and its enhanced westerly winds on 24 November were observed by the in situ GPS dropsonde and Doppler radar measurements from the WP-3D aircraft near the equator (Figs. 4c and 6). A strong westerly jet was associated with the large complex system with multiple MCSs (Fig. 6a) descending from the mid–upper troposphere to the surface (Figs. 6b and 6c). The descending jet coincided with the large areas of the stratiform precipitation as observed by the WP-3D Doppler radar reflectivity and downward velocity as shown in Fig. 6b. Although the type of rear inflow associated with organized MCSs has been observed by Zipser (1977) and Smull and Houze (1987), the very large spatial scale of the descending jet observed by the dropsonde data from 72° to 79°E (>700 km; Fig. 6c) in this case has not been documented prior to DYNAMO. It is interesting to note that, from the Doppler radar reflectivity and velocity data, multiple MCSs were observed along the WP-3D transect from Research Vessel (R/V) *Revelle* to Gan Island (Fig. 6b). The radar reflectivity shows bright bands along the long transect and multiple descending jets, including one from the 1–9-km layer between the 400- and 500-km markers and another 1–5-km layer between 250 and 350 km (Fig. 6b).

The large multi-MCS complex produced a strong and deep cold pool (>4 K in potential temperature depression) extending from the ocean surface up to the 1000-m level (Fig. 6c). Both the enhanced surface westerly wind and the convective cold pools were also captured by the observations at the R/V *Revelle* (Moum et al. 2014). These observations indicate that the MCSs may enhance the surface westerlies during the active phase of the MJO (e.g., Houze et al. 2000), prolong the surface temperature recovery via convective cold pools, and enhance wind-induced upper-ocean mixing (Moum et al. 2014). Thus, these convective upscaling effects of the MCSs may play

an important role in MJO initiation over the tropical Indian Ocean.

Dual aircraft observations of three-dimensional structure of a convective cloud system during the suppressed phase. The WP-3D and Falcon 20 aircraft flew a coordinated mission on 8 December 2011 (Fig. 4d). An example of the dual aircraft measurements in a convective cloud system near Gan Island is presented here (Fig. 7). The mission was designed to characterize the 3D structure of convective cloud systems, including the dynamic, thermodynamic, and microphysical properties. This is a unique dataset for cloud-resolving model evaluation and verification. Figure 8 shows a cross section along the coincident flight paths that was extracted from the 3D gridded WP-3D X-band (3.22 cm) tail Doppler radar data by projecting the WP-3D data onto the Falcon 20 W-band (3.19 mm) Doppler radar data grid using a bilinear interpolation scheme. Because of the increased sensitivity of the Falcon 20 measurements for smaller precipitation particles, observations where reflectivity was less than 15 dBZ were removed for the WP-3D reflectivity and wind fields. For the preliminary view presented here, the fields were simply overlaid. While wind field magnitudes are very close, it can be seen that minor directional discrepancies exist where the two fields merge. This is not surprising given that each instrument has an

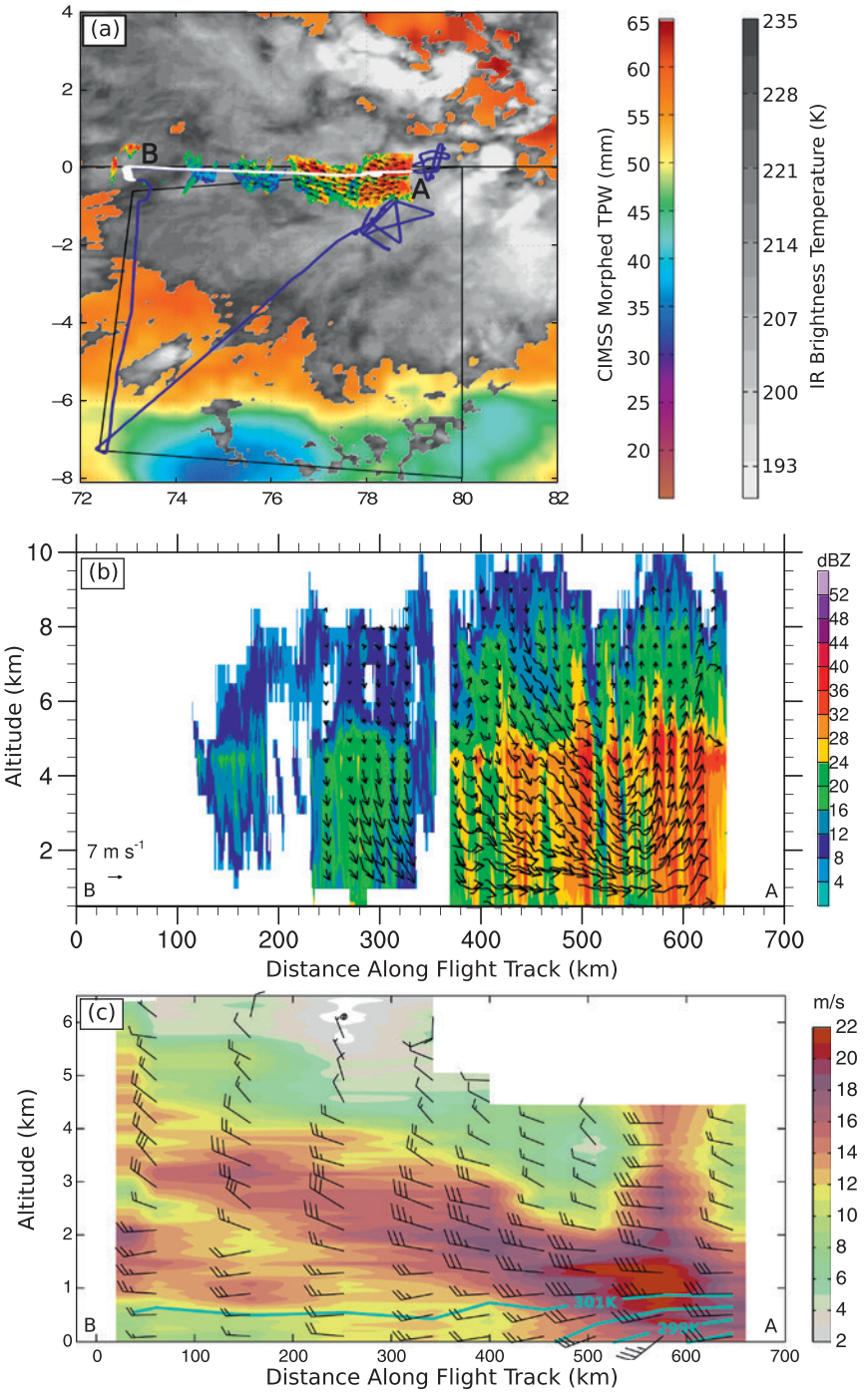

Fig. 6. A large equatorial convective complex with multiple MCSs observed during the active phase of the MJO on 24 Nov: (a) TPW (color, mm) and *Meteosat*-7 IR (gray, K), overlaid with the WP-3D track (white line) and Doppler radar reflectivity (color, dBZ) and wind at the 2-km level. Vertical sections of (b) show the WP-3D reflectivity and horizontal wind vector and (c) wind speed (color, m s^{-1}) and potential temperature (cyan contours from 298 to 301 K with 1-K intervals) from the dropsondes deployed from the WP-3D along the flight leg B–A near the equator [white line in (a)] from 0810 to 0934 UTC 24 Nov.

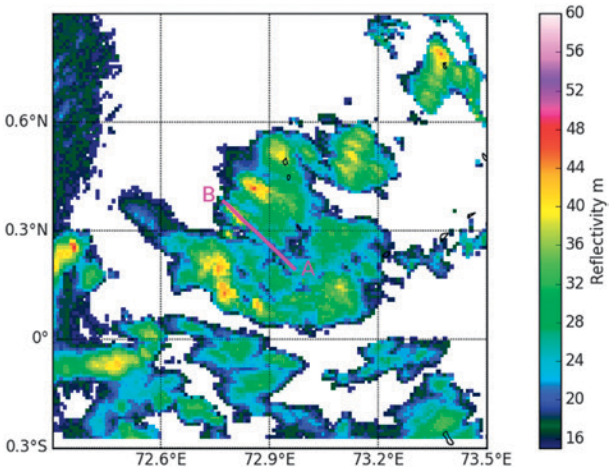

Fig. 7. The coincident flight track of the WP-3D and Falcon 20 aircraft (magenta line) is shown for 0753–0757 UTC 8 Dec 2011. The color contours represent radar reflectivity obtained from the lower fuselage radar aboard the WP-3D.

ideal performance window that becomes decreasingly reliable at this intersection. To improve the analysis going forward, a weighted averaging technique using the magnitudes of reflectivity (or perhaps uncertainties) at each individual point and surrounding eight adjacent neighboring points will be employed to smooth the data at this interface.

The combined vertical cross section of wind shows vertical wind shear within the MCS observed on 8 December (Fig. 8c). This feature is consistent with the observation from the DYNAMO sounding array, which showed strong easterlies in the upper troposphere and moderate westerlies during this time (Johnson and Ciesielski 2013). Understanding how the vertical motion in convective cloud systems interacts with the large-scale horizontal winds in the different phases of the MJO initiation requires synthesis of multiple observational platforms and data sources like in this case.

DISTINCT CONVECTIVE STRUCTURE AND MICROPHYSICS IN THREE MJO PHASES. Sampling from all phases of MJO initiation allowed us to compare the convective structure and microphysical properties of MCSs in different large-scale conditions. The WP-3D Doppler radar reflectivity data were processed from radar convective element (RCE) modules as described in Guy and Jorgensen (2014). Distributions of the height of radar echo tops and the level of maximum reflectivity from the transition/onset phase on 22 November, the convectively active phase on 24 November, and the convectively suppressed phase on 8 December are shown in Fig. 9. It includes a total of six RCEs with two from each of the three days. Although some echo tops reached 13–14-km height in all cases, the echo tops were mainly below 5–6 km during the suppressed phase on 8 December (Fig. 9c) but higher than 10 km in the transition/onset and active periods from 22 to 24 November (Figs. 9a and 9b). A pronounced maximum in peak reflectivity near the melting level (4.5–5.5 km) indicated stratiform precipitation in the convective onset and active cases (Figs. 9d and 9e), which is in strong contrast to that of the suppressed case (Fig. 9f). The highest echo tops and the largest stratiform region were observed during the active phase on 24 November (Fig. 9b), in agreement with the ground-based observation of Zuluaga and Houze (2013). The dry environment in the suppressed phase (Fig. 4d) may have contributed to the relatively shallower convective cells and the lack of stratiform precipitation in the MCSs of 8 December. A similar relationship between environmental moisture and depth of convection was observed during TOGA COARE (Brown and Zhang 1997).

In situ measurements of water droplets were obtained using a combination of optical spectrometers mounted under the left wing of the WP-3D aircraft. The cloud imaging probe (CIP) and the precipitation imaging probe (PIP) measured the particle size and shape between 25 μm–1.55 mm and 100 μm–6.2 mm, respectively. Data were collected during each flight shown in Fig. 1a, with the exception of 11 November due to system errors. These data were largely collected at flight levels typically from 1500 to 3000 m. Raindrop size distributions (RSDs; Jackson and McFarquhar 2014) were produced for each flight. A three-parameter gamma distribution model was used to fit the RSD data. Analysis was performed using a normalized RSD to reduce the impact of mathematical artifacts possible from the highly correlated nature of the parameters of the gamma distribution fit model and removal of a priori shape constraints.

The observed droplet sizes tended to be larger on 22 and 24 November during the onset and active phases than the suppressed periods on 16 November and 8 December (Fig. 10a). This is consistent with the corresponding convective organization on 22–24 November and 8 December shown in Fig. 9. The onset–active phase was characterized by MCSs with broad stratiform regions and embedded deep convective cells (Guy and Jorgensen 2014). This resulted in an enhanced dependence on ice-phase hydrometeor growth, leading to larger D_m of melted drops and

broadening the distribution. Warm rain microphysics dominated during this regime. The 16 November case was sampled in MCSs from 8° to 10°S within the ITCZ during the suppressed phase and exhibited behavior in between the extremes in contrasting MJO phases. The probability distribution of the generalized intercept parameter (N_w) in Fig. 10b indicated the general similarity of systems observed during DYNAMO: namely, an embedded MCS archetype that tends toward the "transition" state between the classically defined convective and stratiform rain regimes. The 8 December case exhibited slightly greater probabilities of higher N_w, though all were within previous maritime measurement variability. The secondary peak on 8 December corresponds to small particles measured by the CIP.

These data can also be used to calculate reflectivity (Z) and rainfall rate (R) using moments of the RSD spectrum. Calculations of Z–R power-law relationships were found to be similar to those found in previous tropical ocean experiments (e.g., TOGA COARE). The imaging probe dataset also allowed for a unique look at the vertical structure of RSDs, which has been sparsely studied. Further work is underway to develop a full understanding of the RSD variations during DYNAMO measured by aircraft (N. Guy et al. 2015, personal communication).

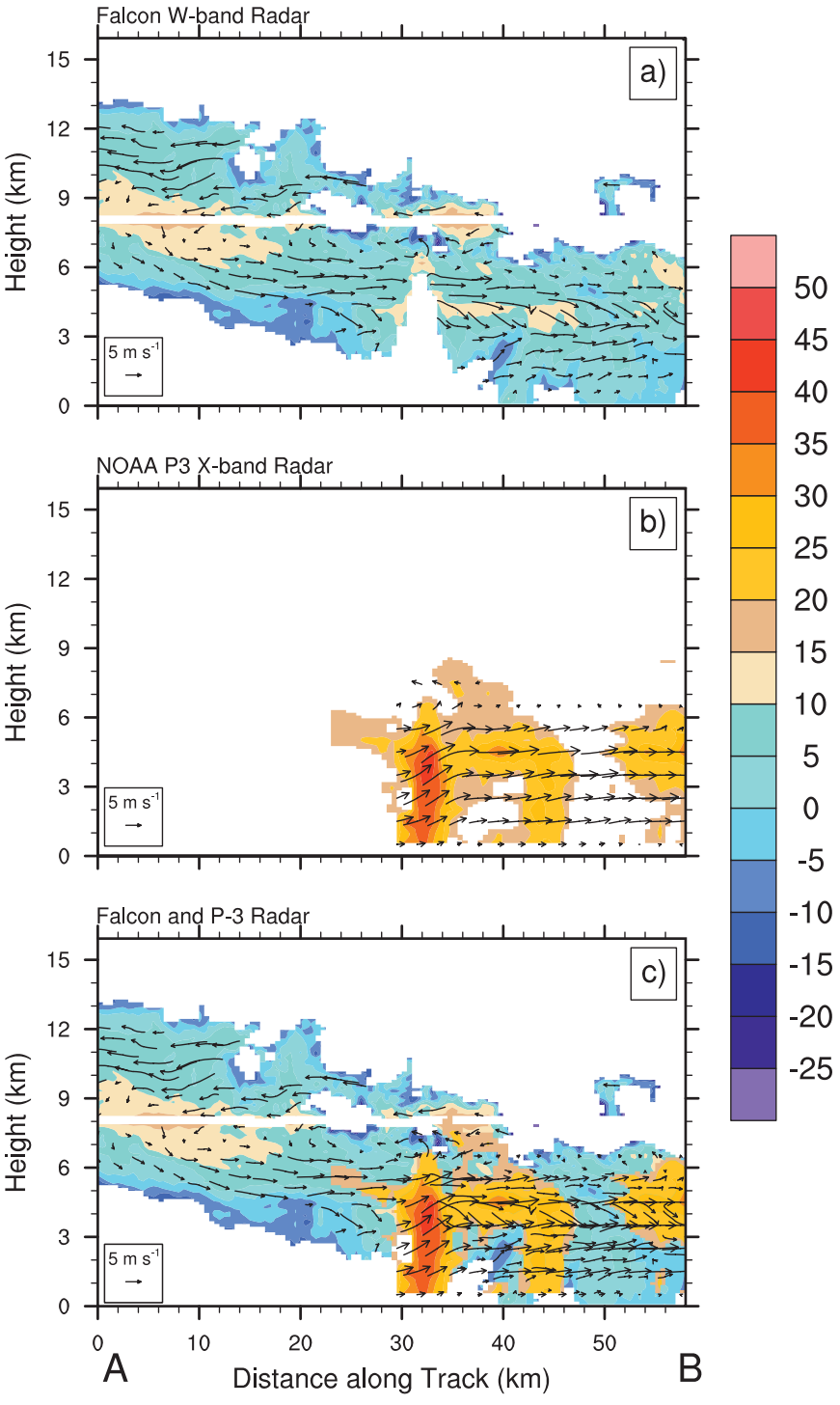

Fig. 8. Vertically pointing (a) Falcon 20 and (b) WP-3D Doppler radar reflectivity (colored contours, dBZ) coincident measurements from 0753 to 0757 UTC 8 Dec 2011 near Gan Island (see Fig. 7) are combined into (c) a coherent vertical cross section. The different radar wavelengths are sensitive to different size particles, allowing for a more detailed picture of the convective system. The overlaid arrows represent 3D wind vectors along the 2D vertical cross section computed from Doppler velocities. Scale for wind vectors is shown in the bottom-left corner of each plot. Values below 15 dBZ are not shown for the WP-3D. The coarse temporal (hence spatial)-resolution WP-3D data are interpolated to the Falcon 20 grid to retain the detailed information provided.

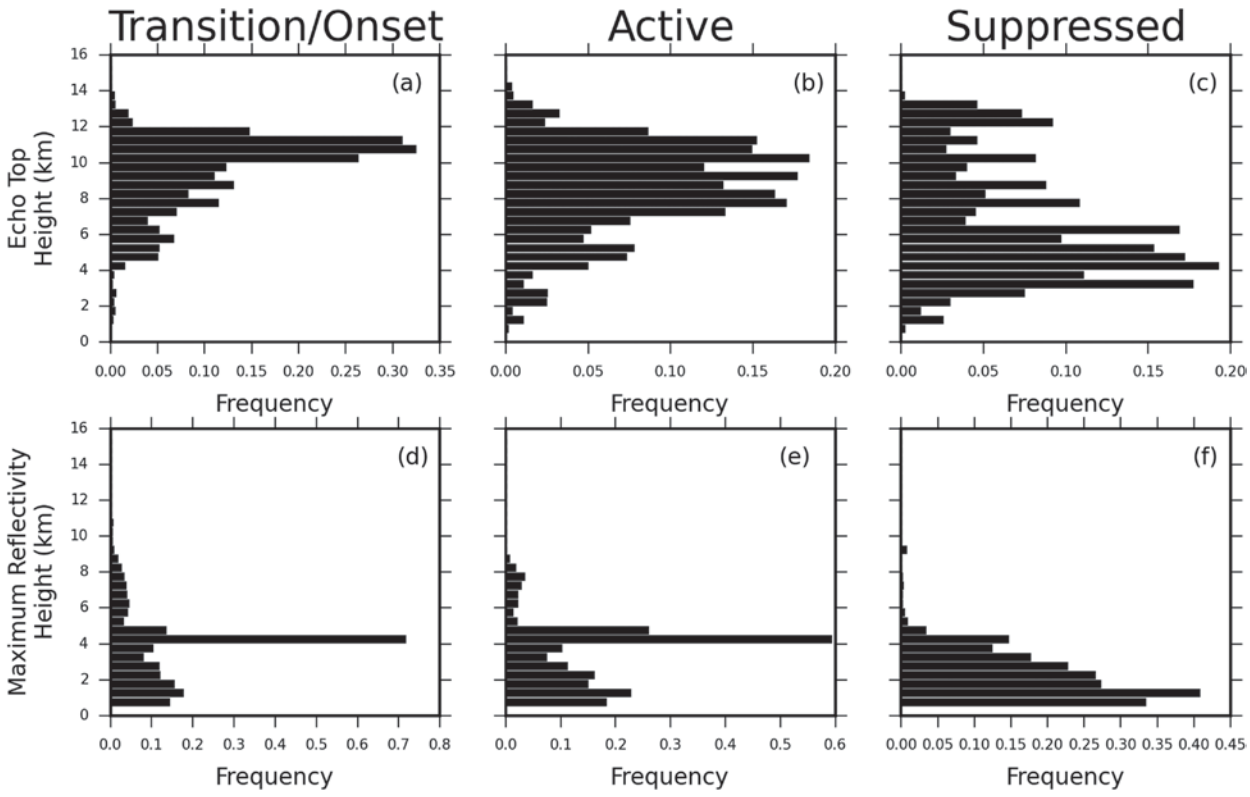

Fig. 9. Frequency of occurrence of (a)–(c) convective echo-top height and (d)–(f) the level of maximum reflectivity observed by the WP-3D Doppler radar during the transition/onset of the equatorial convection on (a),(d) 22 Nov; (b),(e) convectively active phase on 24 Nov; and (c),(f) suppressed phase of the MJO on 8 Dec 2011.

COUPLED OBSERVATIONS OF CONVECTIVELY INDUCED AIR–SEA INTERACTION. It has been hypothesized that air–sea interaction is one of the important factors affecting the equatorial convective cloud systems and the MJO. Chen and Houze (1997a) identified a bidiurnal cycle of large MCSs, referred to as "diurnal dancing," during the MJO active phases over the west Pacific warm pool during TOGA COARE. They speculated that the convective cold pools and large cloud shields have contributed to the slow recovery (>24 h) of the SST and the atmospheric boundary layer after a major convective event. Using satellite-derived SST, wind, and rainfall data, Li and Carbone (2012) showed coherent mesoscale patterns in these fields, suggesting that air–sea coupling plays an important role in the observed rainfall and SST variability over the tropics. However, there are no in situ observations to address the physical processes through which the convection interacts with the ocean and how the air–sea interaction processes vary in different phases of the MJO until DYNAMO. Here we use the aircraft data to examine the coherent variability of the air–sea fluxes and convection during the suppressed and active phases of the MJO over the Indian Ocean. More than 200 collocated GPS dropsonde and AXBT pairs were deployed from the WP-3D aircraft from 11 November to 13 December 2011, which covers the convectively suppressed, transition, and active phases of the MJO.

Convectively induced SST variability. Convective downdrafts and freshwater pools from the rain induce a large spatial and temporal variability in SST, which in turn affects the development of convective cloud systems and air–sea fluxes. During the suppressed phase of the MJO, cool water pools were observed from the infrared camera on board the WP-3D. An example from the WP-3D mission targeting the convective cool pools near Gan Island on 16 November is shown in Fig. 11. The flight track is overlaid on the S-band/Ka-band Dual Polarization, Dual Wavelength Doppler Radar (S-PolKa) reflectivity image, showing isolated small convective cloud systems that the WP-3D was sampling (Fig. 11a). A detailed description of the convective rain cells and associated cold pool signals observed by S-PolKa on 16 November 2011 can be found in Houze et al. (2011). Figures 11b and 11c show a mosaic and spatial series of SST_{skin} variation along

the flight leg marked in red, across a gust front–like feature near convective cells (>40 dBZ; Fig. 11a). The cross-track scale was roughly 1.4 km, and this flight leg spanned roughly 15 km (Figs. 11b and 11c). The small convective systems generated a significant cold pool possibly related to the gust front. Note the two specific features that appear as a pool of cool water and a sharp frontal feature from warm to colder water. The sharp front was detected around 8.5 km into the flight leg. Both of these features may be due to recent rain from the convective cells in the region, as seen in the S-PolKa radar reflectivity (Fig. 11a; see sidebar for additional information on rain, cold pools, and ocean surface during DYNAMO). Although it is difficult to obtain absolute SST_{skin} without ambient measurements, the temperature gradient of nearly 1°C across the flight leg is a robust signal with the effects of window and atmosphere having been removed. Within the cold pool on the ocean surface, the small-scale temperature variability is about 0.1°C m^{-1}. During the active phase of the MJO, the SST (not shown) is more complex with multiscale variability that may be due to both the convectively induced local winds from downdrafts and rain and is under further investigation.

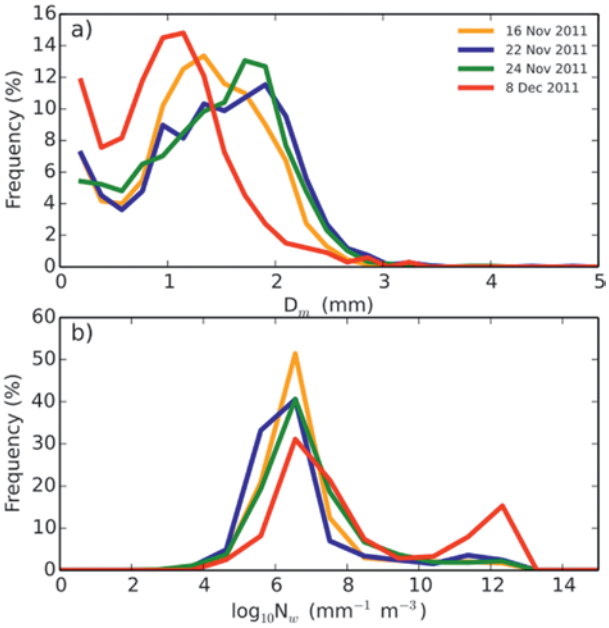

Fig. 10. Probability distributions of (a) mean volume drop diameter and (b) generalized intercept parameter obtained from drop size distributions recorded by the CIP and PIP optical imaging probes aboard the WP-3D aircraft. Suppressed MJO phase/ITCZ on 16 Nov (orange) and 8 Dec (red), MJO onset on 22 Nov (blue), and active MJO phase (green) measurements are shown. The CIP and PIP measurements were made at flight levels typically from 1500 to 3000 m. The corresponding Doppler radar data for 22–24 Nov and 8 Dec are shown in Fig. 9.

Upper-ocean and atmospheric boundary layer temperatures, and air–sea fluxes. One of the sampling strategies of the WP-3D aircraft missions was to observe the atmosphere and ocean environments during both the convectively suppressed and active phases of the MJO. Low-level atmospheric and upper-ocean temperatures were observed by the GPS dropsondes and AXBTs deployed concurrently from the WP-3D aircraft from the southwest–northeast transects between Diego Garcia and the R/V *Revelle* during the convectively suppressed period on 13 November (Fig. 12a) and the active phase on 26 November (Fig. 12b). Three main features are noteworthy. First, the upper-ocean temperature is 2°–3°C warmer during the suppressed phase with weaker winds than the active phase, whereas the atmosphere surface and boundary layer temperatures remained similar. Second, the height of the atmosphere boundary layer (based on the definition of mixed layer using virtual potential temperature < 0.5 K) was higher during the suppressed phase (600–700 m) than in the active phase (500–600 m). Third, there were isolated deep convective clouds along the WP-3D transects on both days, as shown by *Meteosat-7* IR temperatures < 225 K on 13 November (Fig. 12a) and temperatures < 215 K on 26 November (Fig. 12c). However, the convective cold pools were stronger during the suppressed phase (>3°C depression; Fig. 12b) than the active phase (<1.5°C; Fig. 12d). The dryer midlevel to upper-level environmental moisture may be a contributing factor to the stronger cold pools during the suppressed phase (Savarin et al. 2014).

The air–sea sensible and latent heat fluxes are computed from the GPS dropsonde and AXBT measurements using the COARE bulk flux algorithm (Fairall et al. 2003). The sensible heat flux is larger during the suppressed phase on 13 November than the active phase on 26 November over the regions without the influence of convection (from 100 to 750 km; Figs. 12 and 13a). The large surface temperature difference between the air and sea (2°–3°C) and the relatively low wind speed (<5 m s^{-1}) are the main reasons for the higher sensible heat flux during the suppressed phase (Fig. 13b). While the difference in the air–sea mixing ratio was larger on 13 November (suppressed conditions), the latent heat flux was larger on 26 November (active phase) due to the higher wind speed (Figs. 13c and 13d).

Convective cold pools and boundary layer recovery. Convectively generated cold pools can suppress convection by cooling and/or drying the surface and

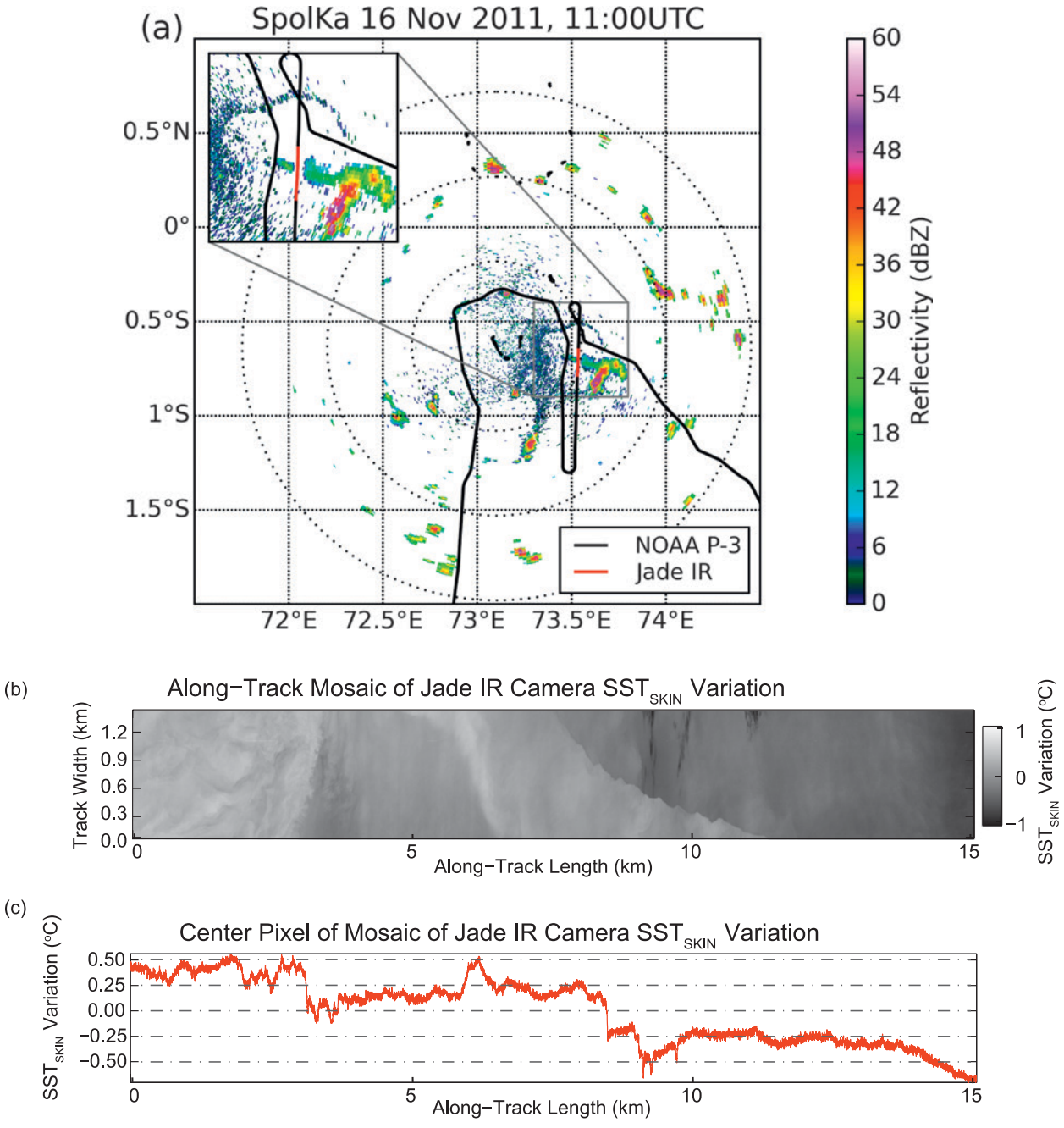

Fig. 11. (a) S-PolKa radar reflectivity at 1100 UTC 16 Nov 2011 (from 0.5° elevation scan) overlaid with the WP-3D flight track (black). The segment of track in red corresponds to 1108:05–1110:00 UTC for the SST_{skin} data shown in (b) and (c). The inset shows a zoomed region near the Jade IR SST measurement. The radial range rings are every 50 km. (b) Mosaic and (c) spatial series of SST_{skin} variation measured from the Jade IR camera on the WP-3D near Gan Island. (Note the large region of cold pool in the mosaic of SST_{skin}.)

boundary layers. Future development of convective cloud systems depends on the recovery of the surface and boundary layers, which is a function of the sunlight and air–sea fluxes. To better understand the air–sea interaction and its impact on convection, we use the aircraft data to investigate both the convectively generated cold pool depth and strength and the boundary layer recovery time during convectively active and suppressed phases of MJO. The WP-3D Doppler radar data were used to identify the convective cloud and precipitation structures that produced the cold pools. The GPS dropsonde data were used to compute the depth and strength of the cold pools, that is, the depth and intensity of negative buoyancy similar

to that described in Bryan et al. (2005). The air–sea fluxes are computed from the GPS dropsonde and AXBT data. To assess the accuracy of the bulk fluxes, we compared the turbulence sensible and latent heat flux data from R/V *Revelle* that overlapped in time with the WP-3D observations in November–December 2011 (C. Fairall and J. Edson 2015, personal communication). The two air–sea flux datasets matched remarkably well. The boundary layer recovery time is then calculated based on the method used in TOGA COARE (Jorgensen et al. 1997), which is the time for the boundary layer properties to recover from the environmental conditions.

In general, the boundary layer recovery times are positively correlated with the surface wind speed and air–sea fluxes (Figs. 14a, 14c, and 14d). Stronger winds and increased air–sea fluxes reduce the recovery time during the convectively active phase, which indicates a positive feedback between the convection and air–sea fluxes. However, the recovery times are longer (5–24 h) during the suppressed phase on 8 December than during the 22–24 November cases (1–13 h; Fig. 14a). The slower recovery time is related to the environmental lower-tropospheric water vapor (700–50-hPa-layer mean RH; Fig. 14b). The depth of the cold pools varies from less than 100 to over 2000 m. The deepest and strongest cold pools were observed in convective cloud systems during the suppressed phase on 8 December (Savarin et al. 2014), which is consistent with the example shown in Fig. 12. The drier the environment the stronger and deeper the cold pools, which is not unexpected given that dry air entrainment by convection can enhance evaporation and convective downdraft. These results may have important implications for the timing of the postconvection surface/boundary layer recovery during an MJO event.

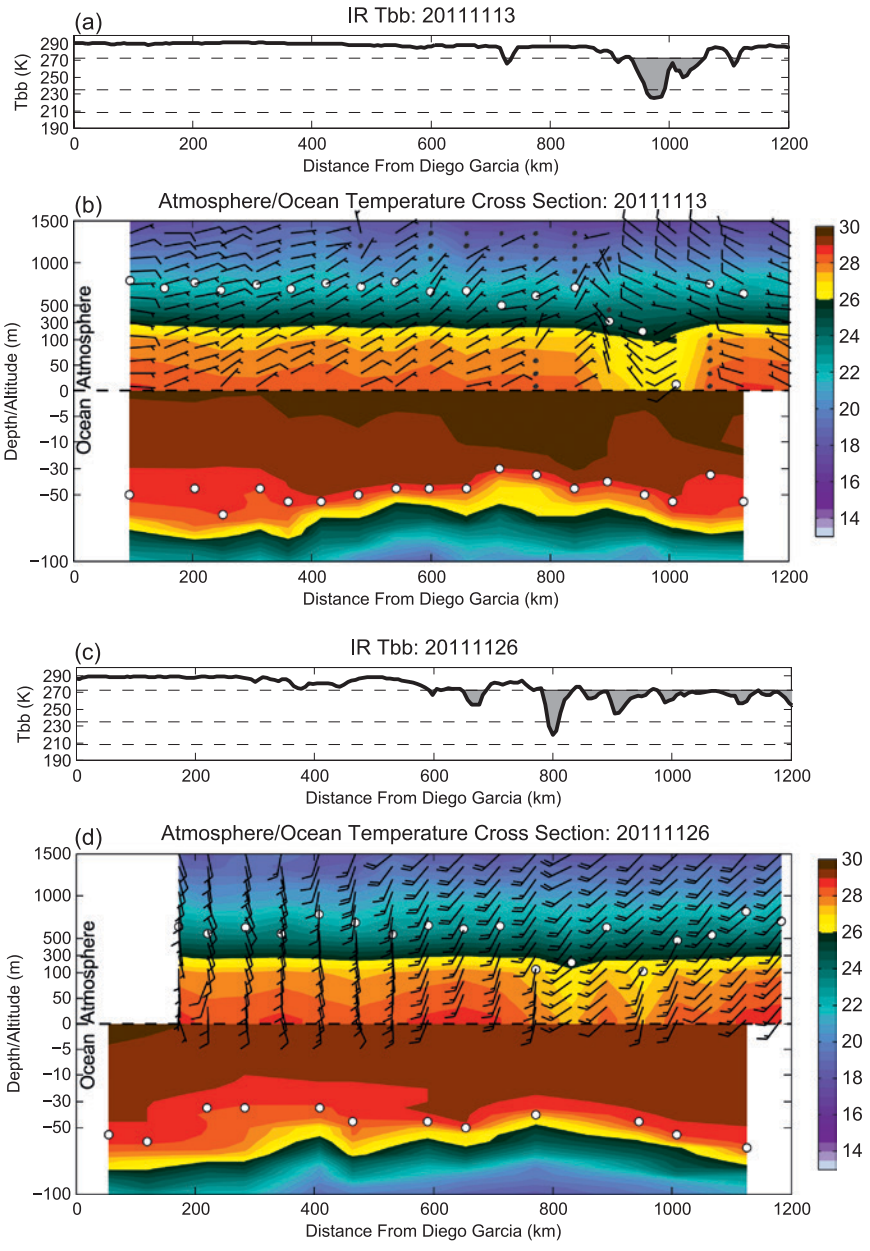

Fig. 12. The *Meteosat*-7 IR cloud-top temperatures (K) and the lower-atmospheric and upper-ocean temperatures (color, °C) measured by the GPS dropsondes and AXBTs deployed from the WP-3D aircraft from transects between Diego Garcia and the R/V *Revelle* during the (a),(b) convectively suppressed phase (13 Nov) and (c),(d) active phase (26 Nov) of the MJO. The depths of the atmosphere and upper-ocean mixed layers are shown by white dots. Note that the altitude in the atmosphere and depth in the ocean are shown in different log scales (m). The wind barbs show the horizontal wind directions and speeds.

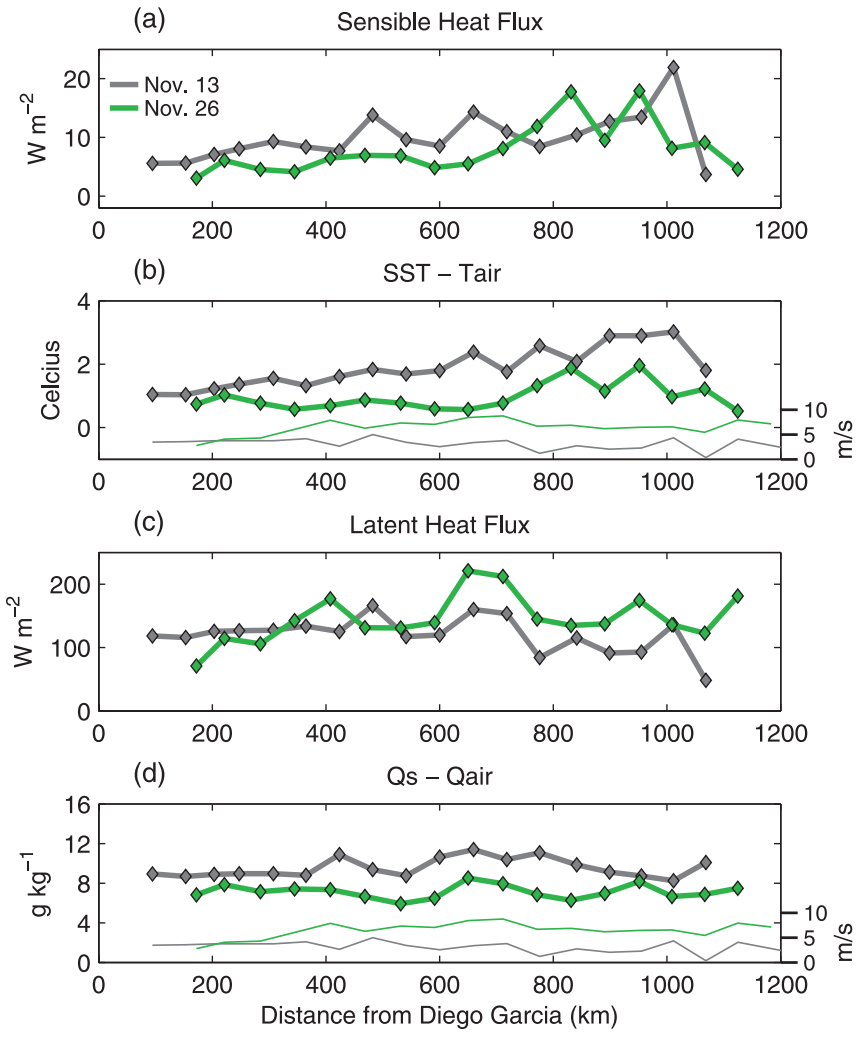

Fig. 13. (a) Air–sea sensible and (c) latent heat fluxes observed using the WP-3D dropsonde and AXBT data from the convectively suppressed phase on 13 Nov (gray) and the active phase on 26 Nov 2011 (green) along the same transects showing in Fig. 12. Corresponding (b) air–sea temperature and (d) specific humidity differences along with the surface wind speeds (m s^{-1}, thin gray and green lines).

- Dry air intrusions from the subtropics may suppress convection in the ITCZ, which is favorable for the onset of the equatorial convection during MJO initiation (Figs. 3–5).
- Distinct characteristics were found in the convective structure and microphysical properties of MCSs during the suppressed, transition/onset, and active phases of the MJO (Figs. 9 and 10).
- Convective cold pools are deeper and stronger in MCSs surrounded by the low–midlevel dry air (Figs. 6, 8, and 14) in the suppressed phase, which prolong the atmosphere boundary layer recovery time.
- The atmospheric boundary layer depth and upper-ocean temperature are higher during the suppressed phase than during the active phase, and the air–sea temperature difference and sensible fluxes (Figs. 12 and 13) are larger during the suppressed phase of the MJO.

These topics deserve further investigation. Collectively they highlight the importance of the atmospheric water vapor variability and its impact on organizations and structure of convective cloud systems, as well as their interaction with the ocean through air–sea fluxes on MJO initiation over the tropical Indian Ocean. The aircraft sampling strategy allowed for coherent observations of MCS structure and microphysics using the Doppler radar and microphysics probes and the large-scale atmospheric and ocean environment using the GPS dropsonde and AXBT measurements, which were not available in TOGA COARE. The dual aircraft measurements by the WP-3D and Falcon 20 Doppler radars provided the first 3D reflectivity and velocity observations from 0.5–15.0-km height. The results shown here will help us improve and evaluate high-resolution, cloud-resolving, and

CONCLUDING REMARKS. The DYNAMO field campaign collected unprecedented aircraft observations over the tropical Indian Ocean during November–December 2011. The mobility of the aircraft proves to be vital in capturing some key features, such as the spatial distribution of the large-scale water vapor and the small-scale SST variations associated with convective cold pools, filling a gap from the ship- and land-based station observations. These observations, in combination with other DYNAMO land-based, shipborne, and satellite data, have provided invaluable new insights into MJO initiation over the tropical Indian Ocean. A number of emerging science topics are highlighted here:

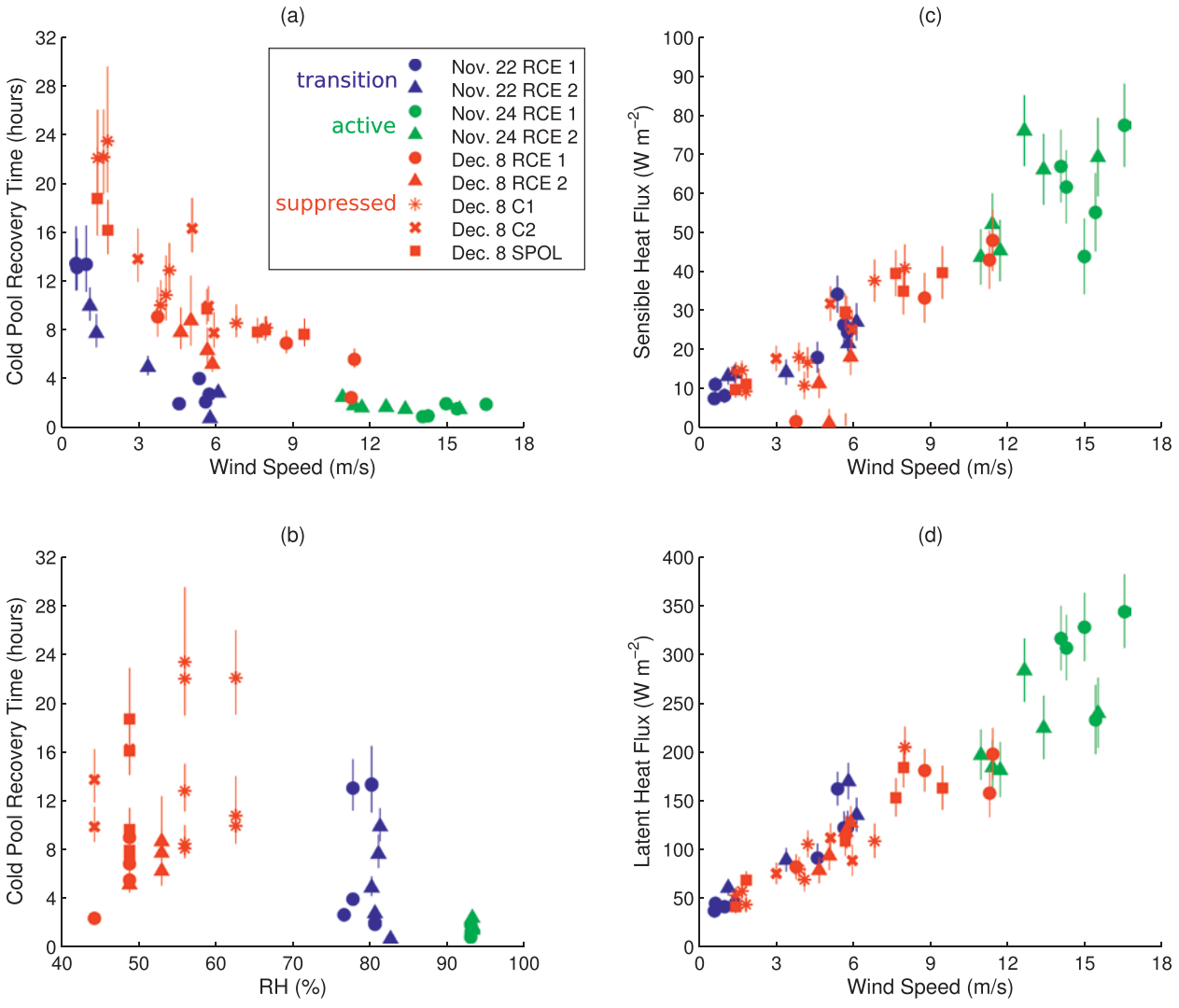

Fig. 14. The WP-3D aircraft observed convective cold pool recovery time varies with (a) wind speed and (b) the 700–500-hPa environment RH averaged over a circular area of 200–500-km radius from each dropsonde. The (c) surface sensible heat and (d) latent heat fluxes varying with wind speed, for individual convective modules from 22 Nov (blue), 24 Nov (green), and 8 Dec 2011 (red), which represent the MJO transition/onset, convectively active, and suppressed phases, respectively. The error bars represent the uncertainty due to SST ±0.5°C and the range of wind speeds within the lowest 50 m.

coupled atmosphere–ocean models for better prediction of MJO initiation processes in the future. The aircraft data have been organized into an easily accessible form made available online (http://data.eol.ucar.edu/master_list/?project=DYNAMO). It is hoped that they will be used by others in studies for better understanding and predicting the MJO and numerical model evaluation and verification.

ACKNOWLEDGMENTS. We thank our colleagues at the NOAA Aircraft Operations Center (AOC; Jim McFadden, the pilots, aircraft crew, and flight directors) and the NCAR Earth Observing Laboratory (EOL; Jim Moore, José Meitín, Scot Loehrer, and others), who provided critical support for operating the aircraft from Diego Garcia and Gan during DYNAMO. We are grateful to Patrick Chuang, Mikael Witte, and Bob Black for their help in processing the microphysics data; Scott Brown for collecting the IR SST imaging data; David Trampp, Jeff Kerling, and Qing Wang for the AXBT data; Tammy Weckwerth and Scott Ellis for helping with the aircraft missions using S-PolKa data near Gan Island; Jeff Hawkins for providing the satellite data in real time; Jon Gottschalck and Nick Hall for real-time forecasting support; and Ed Ryan for assisting with the cloud-cluster tracking during DYNAMO. Aircraft- and ground-based radar images were created using the Py-ART

and AWOT software packages courtesy of the Department of Energy ARM Climate Research facility and the NOAA National Severe Storms Laboratory, respectively. Comments and suggestions from three anonymous reviewers and Dr. Brian Mapes helped improve the manuscript significantly. This research was supported by grants from NOAA (NA11OAR4310077), NSF (AGS1062242), and ONR (N000141110562).

REFERENCES

Benedict, J., and D. A. Randall, 2009: Structure of the Madden–Julian oscillation in the superparameterized CAM. *J. Atmos. Sci.*, **66**, 3277–3296, doi:10.1175/2009JAS3030.1.

Brown, R. G., and C. Zhang, 1997: Variability of midtropospheric moisture and its effect on cloud-top height distribution during TOGA COARE. *J. Atmos. Sci.*, **54**, 2760–2774, doi:10.1175/1520-0469(1997)054<2760:VOMMAI>2.0.CO;2.

Bryan, G., D. Ahijevich, C. Davis, S. Trier, and M. Weisman, 2005: Observations of cold pool properties in mesoscale convective systems during BAMEX. *11th Conf. on Mesoscale Processes*, Hyannis, MA, Amer. Meteor. Soc., JP5J.12. [Available online at https://ams.confex.com/ams/32Rad11Meso/techprogram/paper_96718.htm.]

Chen, S. S., and R. A. Houze, Jr., 1997a: Diurnal variation and lifecycle of deep convective systems over the tropical Pacific warm pool. *Quart. J. Roy. Meteor. Soc.*, **123**, 357–388, doi:10.1002/qj.49712353806.

——, and ——, 1997b: Interannual variability of deep convection over the tropical warm pool. *J. Geophys. Res.*, **102**, 25 783–25 795, doi:10.1029/97JD02238.

——, ——, and B. E. Mapes, 1996: Multiscale variability of deep convection in relation to large-scale circulation in TOGA COARE. *J. Atmos. Sci.*, **53**, 1380–1409, doi:10.1175/1520-0469(1996)053<1380:MVODCI>2.0.CO;2.

Fairall, C. W., E. F. Bradley, J. E. Hare, A. A. Grachev, and J. B. Edson, 2003: Bulk parameterization of air–sea fluxes: Updates and verification for the COARE algorithm. *J. Climate*, **16**, 571–591, doi:10.1175/1520-0442(2003)016<0571:BPOASF>2.0.CO;2.

Gottschalck, J., P. E. Roundy, C. J. Schreck III, A. Vintzileos, and C. Zhang, 2013: Large-scale atmospheric and oceanic conditions during the 2011–12 DYNAMO field campaign. *Mon. Wea. Rev.*, **141**, 4173–4196, doi:10.1175/MWR-D-13-00022.1.

Guy, N., and D. P. Jorgensen, 2014: Kinematic and precipitation characteristics of convective systems observed by airborne Doppler radar during the life cycle of a Madden–Julian oscillation in the Indian Ocean. *Mon. Wea. Rev.*, **142**, 1385–1402, doi:10.1175/MWR-D-13-00252.1.

Houze, R. A., Jr., S. S. Chen, D. Kingsmill, Y. Serra, and S. E. Yuter, 2000: Convection over the Pacific warm pool in relation to the atmospheric Kelvin–Rossby wave. *J. Atmos. Sci.*, **57**, 3058–3089, doi:10.1175/1520-0469(2000)057<3058:COTPWP>2.0.CO;2.

——, H. C. Barns, D. Hence, and K. Chakravarty, 2011: Convective outbreak near Diego Garcia and cold pools near S-PolKa. DYNAMO Field Catalog. [Available online at http://catalog.eol.ucar.edu/cgi-bin/dynamo/htmlwrap?file_url=/dynamo/report/spolkascientist/20111116/report.SPolKaScientist.20111116.science_summary.html.]

Huffman, G. J., and Coauthors, 2007: The TRMM Multisatellite Precipitation Analysis (TMPA): Quasi-global, multiyear, combined-sensor precipitation estimates at fine scales. *J. Hydrometeor.*, **8**, 38–55, doi:10.1175/JHM560.1.

Jackson, R. C., and G. M. McFarquhar, 2014: An assessment of the impact of anti-shattering tips and artifact removal techniques on bulk cloud ice microphysical and optical properties measured by the 2D cloud probe. *J. Atmos. Oceanic Technol.*, **31**, 2131–2144, doi:10.1175/JTECH-D-14-00018.1.

Johnson, R. H., and P. E. Ciesielski, 2013: Structure and properties of Madden–Julian oscillations deduced from DYNAMO sounding arrays. *J. Atmos. Sci.*, **70**, 3157–3179, doi:10.1175/JAS-D-13-065.1.

Jorgensen, D. P., T. Matejka, and J. D. DuGranrut, 1996: Multi-beam techniques for deriving wind fields from airborne Doppler radars. *Meteor. Atmos. Phys.*, **59**, 83–104, doi:10.1007/BF01032002.

——, M. A. LeMone, and S. B. Trier, 1997: Structure and evolution of the 22 February 1993 TOGA-COARE squall line: Aircraft observations of precipitation, circulation, and surface energy fluxes. *J. Atmos. Sci.*, **54**, 1961–1985, doi:10.1175/1520-0469(1997)054<1961:SAEOTF>2.0.CO;2.

Judt, F., and S. S. Chen, 2014: An explosive convective cloud system and its environmental conditions in MJO initiation observed during DYNAMO. *J. Geophys. Res. Atmos.*, **119**, 2781–2795, doi:10.1002/2013JD021048.

Kerns, B. W., and S. S. Chen, 2014a: ECMWF and GFS model forecast verification during DYNAMO: Multiscale variability in MJO initiation over the equatorial Indian Ocean. *J. Geophys. Res. Atmos.*, **119**, 3736–3755, doi:10.1002/2013JD020833.

——, and ——, 2014b: Equatorial dry air intrusion and related synoptic variability in MJO initiation during DYNAMO. *Mon. Wea. Rev.*, **142**, 1326–1343, doi:10.1175/MWR-D-13-00159.1.

Kiladis, G. N., M. C. Wheeler, P. T. Haertel, K. H. Straub, and P. E. Roundy, 2009: Convectively coupled equatorial waves. *Rev. Geophys.*, **47**, RG2003, doi:10.1029/2008RG000266.

Li, Y., and R. E. Carbone, 2012: Excitation of rainfall over the tropical western Pacific. *J. Atmos. Sci.*, **69**, 2983–2994, doi:10.1175/JAS-D-11-0245.1.

Madden, R. A., and P. R. Julian, 1971: Detection of a 40–50 day oscillation in the zonal wind in the tropical Pacific. *J. Atmos. Sci.*, **28**, 702–708, doi:10.1175/1520-0469(1971)028<0702:DOADOI>2.0.CO;2.

——, and ——, 1972: Description of global-scale circulation cells in the tropics with a 40–50 day period. *J. Atmos. Sci.*, **29**, 1109–1123, doi:10.1175/1520-0469(1972)029<1109:DOGSCC>2.0.CO;2.

Maloney, E. D., and D. L. Hartmann, 2000: Modulation of hurricane activity in the Gulf of Mexico by the Madden-Julian Oscillation. *Science*, **287**, 2002–2004, doi:10.1126/science.287.5460.2002.

Mechem, D. B., S. S. Chen, and R. A. Houze Jr., 2005: Momentum transport processes in the stratiform regions of mesoscale convective systems over the western Pacific warm pool. *Quart. J. Roy. Meteor. Soc.*, **132A**, 709–736, doi:10.1256/qj.04.141.

Moum, J. N., and Coauthors, 2014: Air–sea interactions from westerly wind bursts during the November 2011 MJO in the Indian Ocean. *Bull. Amer. Meteor. Soc.*, **95**, 1185–1199, doi:10.1175/BAMS-D-12-00225.1.

Savarin, A., S. S. Chen, B. W. Kerns, and D. P. Jorgensen, 2014: Convective cold pool structure and boundary layer recovery time in DYNAMO. *31st Conf. on Hurricanes and Tropical Meteorology*, San Diego, CA, Amer. Meteor. Soc., 9B.2. [Available online at https://ams.confex.com/ams/31Hurr/webprogram/Paper245387.html.]

Smull, B. F., and R. A. Houze Jr., 1987: Rear inflow in squall lines with trailing stratiform precipitation. *Mon. Wea. Rev.*, **115**, 2869–2889, doi:10.1175/1520-0493(1987)115<2869:RIISLW>2.0.CO;2.

Stephens, G. L., P. J. Webster, R. H. Johnson, R. Engelen, and T. S. L'Ecuyer, 2004: Observational evidence for the mutual regulation of the tropical hydrological cycle and tropical sea surface temperatures. *J. Climate*, **17**, 2213–2224, doi:10.1175/1520-0442(2004)017<2213:OEFTMR>2.0.CO;2.

Yoneyama, K., and D. B. Parsons, 1999: A proposed mechanism for the intrusion of dry air into the tropical western Pacific region. *J. Atmos. Sci.*, **56**, 1524–1546, doi:10.1175/1520-0469(1999)056<1524:APMFTI>2.0.CO;2.

——, C. Zhang, and C. N. Long, 2013: Tracking pulses of the Madden–Julian oscillation. *Bull. Amer. Meteor. Soc.*, **94**, 1871–1891, doi:10.1175/BAMS-D-12-00157.1.

Zhang, C., 2013: Madden–Julian oscillation: Bridging weather and climate. *Bull. Amer. Meteor. Soc.*, **94**, 1849–1870, doi:10.1175/BAMS-D-12-00026.1.

Zhang, H.-M., J. J. Bates, and R. W. Reynolds, 2006: Assessment of composite global sampling: Sea surface wind speed. *Geophys. Res. Lett.*, **33**, L17714, doi:10.1029/2006GL027086.

Zhou, S., M. L'Heureux, S. Weaver, and A. Kumar, 2012: A composite study of the MJO influence on the surface air temperature and precipitation over the continental United States. *Climate Dyn.*, **38**, 1459–1471, doi:10.1007/s00382-011-1001-9.

Zipser, E. J., 1977: Mesoscale and convective-scale downdrafts as distinct components of squall line structure. *Mon. Wea. Rev.*, **105**, 1568–1589, doi:10.1175/1520-0493(1977)105<1568:MACDAD>2.0.CO;2.

Zuluaga, M. D., and R. A. Houze, 2013: Evolution of the population of precipitating convective systems over the equatorial Indian Ocean in active phases of the Madden–Julian oscillation. *J. Atmos. Sci.*, **70**, 2713–2725, doi:10.1175/JAS-D-12-0311.1.

EYEWITNESS

Evolution of the Atmospheric Sciences

by ROBERT G. FLEAGLE

Eyewitness: Evolution of the Atmospheric Sciences describes how the atmospheric sciences were transformed in the span of the author's professional career from its origins in primitive weather forecasting to its current focus on numerical modeling of environmental change. It describes the author's observations of persons, events, and institutions beginning with graduate study during the Second World War and moving on to continuing expansion of the atmospheric sciences and technologies, through development of a major university department, development of new scientific and professional institutions, and to the role that the science of the atmosphere now plays in climate change and other issues of social and political policy.

Photo ©Kathy Sauber/University of Washington

EYEWITNESS: EVOLUTION OF THE ATMOSPHERIC SCIENCES

ISBN 1-878220-39-X, 129 pp., hardbound, $75 list/$55 member.

Order online: www.ametsoc.org/amsbookstore

or see the order form at the back of this issue.

ABOUT THE AUTHOR

Robert G. Fleagle earned degrees in physics and meteorology at The Johns Hopkins University and New York University and began his professional career in 1948 at the University of Washington (UW). His research has focused on the structure of midlatitude cyclones, the physics and structure of the surface boundary layer, and processes of air–sea interaction. He is the author of about 100 papers published in scientific journals and of books on atmospheric physics and global environmental change. Applications of science to social and political policy have been important motivations for his career and have occupied his attention increasingly as the decades passed.

Fleagle participated at close range in the beginnings and growth of a major university department and of the University Corporation for Atmospheric Research (UCAR). In 1963 and 1964 he served as a staff specialist in the Office of Science and Technology, Executive Office of the President, and in 1977–78 he served as consultant to the National Oceanic and Atmospheric Administration. He has held many administrative posts including chairman of the UW Department of Atmospheric Sciences (1967–77), chairman of the National Academy of Sciences Committee on Atmospheric Sciences (1969–73),